

# Deep Learning Based Detection and Correction of Cardiac MR Motion Artefacts During Reconstruction for High-Quality Segmentation

Ilkay Oksuz, James R. Clough, Bram Ruijsink, Esther Puyol-Antón, Aurelien Bustin, Gastao Cruz, Claudia Prieto, Andrew P. King, Julia A. Schnabel

**Abstract**—Segmenting anatomical structures in medical images has been successfully addressed with deep learning methods for a range of applications. However, this success is heavily dependent on the quality of the image that is being segmented. A commonly neglected point in the medical image analysis community is the vast amount of clinical images that have severe image artefacts due to organ motion, movement of the patient and/or image acquisition related issues. In this paper, we discuss the implications of image motion artefacts on cardiac MR segmentation and compare a variety of approaches for jointly correcting for artefacts and segmenting the cardiac cavity. The method is based on our recently developed joint artefact detection and reconstruction method, which reconstructs high quality MR images from k-space using a joint loss function and essentially converts the artefact correction task to an under-sampled image reconstruction task by enforcing a data consistency term. In this paper, we propose to use a segmentation network coupled with this in an end-to-end framework. Our training optimises three different tasks: 1) image artefact detection, 2) artefact correction and 3) image segmentation. We train the reconstruction network to automatically correct for motion-related artefacts using synthetically corrupted cardiac MR k-space data and uncorrected reconstructed images. Using a test set of 500 2D+time cine MR acquisitions from the UK Biobank data set, we achieve demonstrably good image quality and high segmentation accuracy in the presence of synthetic motion artefacts. We quantitatively compare our method with a variety of techniques for jointly recovering image quality and performing image segmentation. We showcase better performance compared to state-of-the-art image correction techniques. Moreover, our method preserves the quality of uncorrupted images and therefore can be utilised as a global image reconstruction algorithm.

**Index Terms**—Image Quality, Image Segmentation, Deep Learning, Cardiac MRI, Image artifacts

## I. INTRODUCTION

**I**MAGE reconstruction, image denoising and down-stream tasks (e.g. registration and segmentation) are traditionally

considered as three separate tasks in medical image analysis. Medical image analysis techniques are typically applied to the raw data in a serial fashion, which can introduce a cascade of errors from one task to the next, particularly when the quality of the acquired data is low. While medical image analysis is taking an increasingly important role in clinical decision making, an often neglected step in automated image analysis pipelines is the assurance of image quality. This is an important step because high accuracy in downstream tasks such as segmentation depends strongly on high quality medical images [1].

Cine cardiac magnetic resonance (CMR) images are routinely acquired for the assessment of cardiac health, and can be used to derive metrics of cardiac function including volume, ejection fraction and strain [2], as well as to investigate local myocardial wall motion abnormalities. CMR images are often acquired in patients who already have existing cardiovascular disease. These patients are more likely to have arrhythmias or have difficulties with either breath-holding or remaining still during acquisition. Therefore, the images can contain a range of image artefacts [3], and assessing the quality of images acquired by MR scanners is a challenging problem. Misleading segmentations can be the result and can lead clinicians to draw incorrect conclusions from the imaging data [4]. In current clinical practice, images are visually inspected by one or more experts, and those of insufficient quality are excluded from further analysis and/or reacquired. However, if successful image correction and segmentation algorithms are in place, these data could be utilised for further clinical evaluation.

In this paper, we propose a deep learning based approach for a fully automated framework for joint motion artefact detection, correction and segmentation in cine CMR short axis images. A novel end-to-end training setup is proposed to detect and correct motion artefacts and extract segmentations for the corrected images in a comprehensive, integrated framework. An analysis of multiple deep learning architectures and learning mechanisms is also presented. This paper builds upon our previously presented work [4], in which we proposed the use of a Convolutional Neural Network (CNN) architecture to both detect and correct motion artefacts. Here, we extend this idea to a joint training approach for image artefact detection, correction and segmentation.

Our algorithm is capable of producing high quality images and corresponding high quality segmentations from low quality acquired data. An example of an artefact-corrected

Copyright (c) 2019 IEEE. Personal use of this material is permitted. However, permission to use this material for any other purposes must be obtained from the IEEE by sending a request to pubs-permissions@ieee.org.

This work was supported by an EPSRC programme Grant (EP/P001009/1) and the Wellcome EPSRC Centre for Medical Engineering at the School of Biomedical Engineering and Imaging Sciences, Kings College London (WT 203148/Z/16/Z). This research has been conducted using the UK Biobank Resource under Application Number 17806. The GPU used in this research was generously donated by the NVIDIA Corporation. Correspondence to I. Oksuz.

I. Oksuz, J. R. Clough, Bram Ruijsink, Esther Puyol-Antón, Aurelien Bustin, Gastao Cruz, Claudia Prieto, Andrew P. King, Julia A. Schnabel are with School of Biomedical Engineering and Imaging Sciences, King's College London, London, UK e-mail: (ilkay.oksuz@kcl.ac.uk).

image is shown in Figure 1b and its corresponding high quality segmentation in Figure 1e. The original images corrupted with motion and its segmentation can be seen in Figures 1a and 1d

The remainder of this paper is organised as follows. In Section II, we first present an overview of the relevant literature in image artefact detection and correction. Then, we review the literature on simultaneous image correction and downstream tasks, and present our novel contributions in this context. In Section III, we provide details of the clinical data sets used. In Section IV we describe our proposed framework for image artefact detection, correction and segmentation including descriptions of the novel loss functions. Results are presented in Section V, while Section VI summarises the findings of this paper in the context of the literature and proposes potential directions for future work.

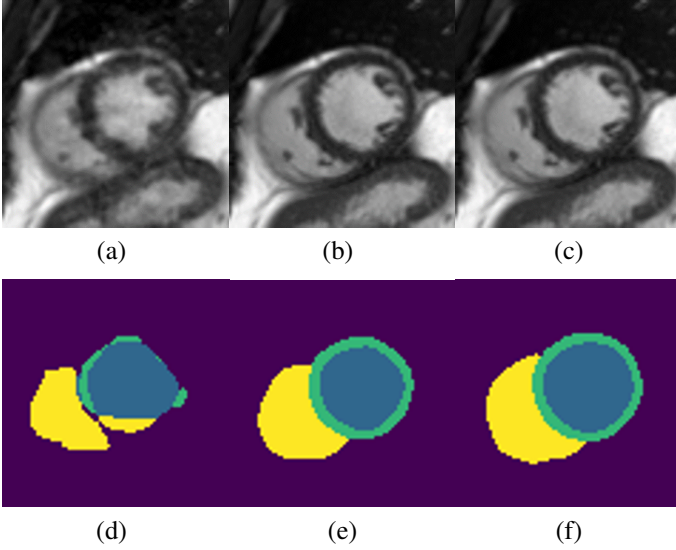


Fig. 1. Examples of a low quality cine CMR image (a) and its corresponding segmentation achieved (d) by a U-net [5] trained on low quality images. We applied our framework to detect and correct the image and achieved image (b) and segmentation (e), which are close to ground truth image (c) and segmentation (f).

## II. RELATED WORKS

In this section, we provide an overview of the relevant literature on image quality assesment, image artefact correction and end-to-end training for down-stream analysis of low quality images with a focus on applications in medical image analysis.

### A. Image quality assessment

Image quality assessment (IQA) has been an active area of research in computer vision and deep learning methods have shown great success on benchmark data sets [6]. IQA is a vital step for analysing large medical image data sets as detailed in [7]. Early efforts in medical imaging focused on quantifying the image quality of brain MR images [8]. The success of deep learning has motivated the medical image analysis community to utilise such methods on multiple image

quality assessment challenges such as fetal ultrasound [9] and echocardiography [10] using 2D images and pre-trained networks. Kuestner et al. [11] utilised a patch-based CNN architecture to detect motion artefacts in head and abdominal MR scans to achieve spatially-aware probability maps. In more recent work, [12] proposed to utilise a variety of features and trained a deep neural network for artefact detection.

CMR image quality issues have mostly been studied in the context of missing slices [13], due to their adverse influence on calculating ventricular volume, and therefore, ejection fraction. Tarroni et al. [14] proposed the use of a decision forest approach for heart coverage estimation, inter-slice motion detection and image contrast estimation in the cardiac region. CMR image quality has also been linked with automatic quality control of image segmentation in [15]. In a comprehensive segmentation framework, Alba et al. proposed to use a random forest classifier to eliminate failed myocardial segmentation [16]. The authors of [17] investigated synthetic motion artefacts and used histogram, box, line and texture features to train a random forest algorithm to detect different artefact levels. In a more recent work, Oksuz et al. [18] proposed to use a curriculum learning strategy exploiting different levels of k-space corruption to detect cardiac motion artefacts. All of these techniques only detect the artefacts and do not correct the artefact-corrupted data. Therefore, they can be used as a rejection mechanism in clinical scenarios but cannot allow utilisation of corrupted data.

### B. Image artefact correction

To make full use of available clinical databases, image artefact correction methods are instrumental as they help ensure that all images meet the same high standard of image quality. The use of deep learning based image reconstruction to increase the quality of MR imaging under accelerated acquisition has been of recent interest to the community [19]. Deep learning has recently shown great promise in the reconstruction of highly undersampled MR acquisitions with CNNs [20], [21]. In a pioneering work, Schlemper et al. [21] proposed to use a deep cascaded network to generate high quality images, and Hauptmann et al. [22] proposed to use a residual U-net to reduce aliasing artefacts due to undersampling, with the purpose of accelerating image acquisition. Our work aims to exploit the advances made in these methods in the context of artefact-corrupted data, and to further extend the framework to encompass the common downstream task of image segmentation.

### C. End-to-end techniques

The idea of addressing the problems of image quality and coupling them with downstream tasks (e.g. segmentation) has been proven to be effective in the computer vision literature [23]. Application-driven image denoising networks can even be trained without ground truth segmentations as illustrated in [24].

Deep learning techniques have been utilised for segmentation problems with high success [25]. However, the influence of variability in acquisition protocols, pathology and image artefacts is an often overlooked problem. In a recent work, Shao et al. [26] demonstrated the shortcomings of deep learning in the presence of pathology for brain MR segmentation with an emphasis on the selection of training data.

In particular for medical imaging, combining reconstruction and segmentation has proven to be effective for undersampled k-space image acquisitions for cardiac MR [27] and brain MR [28]. Schlemper et al. [29] proposed a technique that can generate segmentations using fewer than 10 k-space lines. Similar techniques have been proposed to fuse super-resolution and cardiac MR segmentation [30] by using anatomical constraints through auto-encoders. More recently, Sun et al. [31] proposed using multiple cascaded blocks with the same encoder to simultaneously reconstruct and segment brain MR from undersampled k-space acquisitions. Our work differs from these methods, which focus on undersampling for acceleration. We focus on artefacts and aim for improved quality of images and segmentations. To the best of our knowledge, our work is the first that has investigated joint image artefact detection, correction and segmentation in a single pipeline for CMR. We demonstrate application of the framework to CMR but we believe it could also offer benefits to brain MR or other applications.

#### D. Contributions

There are four major contributions of this work:

- To the authors' knowledge, this is the first paper that detects, corrects and segments cardiac MR images with motion artefacts in a unified framework directly from k-space;
- We present an extensive analysis of segmentation of low quality cardiac images with various deep learning architectures;
- Our framework does not diminish the quality of high quality images and increases the quality of low quality images;
- We prospectively analyse performance on a testing case to illustrate the potential of our technique for image artefact correction and segmentation.

This paper builds upon two previous works: 1) our unified network for image artefact detection and correction [4], and 2) our investigation of the influence of low quality images on the final segmentation result using a comparison of various artefact correction strategies [1]. Here, we extend the of idea of detecting and correcting the image artefacts in a single framework by incorporating a segmentation network and performing joint training of our pipeline.

### III. MATERIALS

In this section, we detail the data set that is used to train and test our framework. We also discuss the synthetic image artefact generation mechanism to establish coupled low quality and high quality data to train our method.

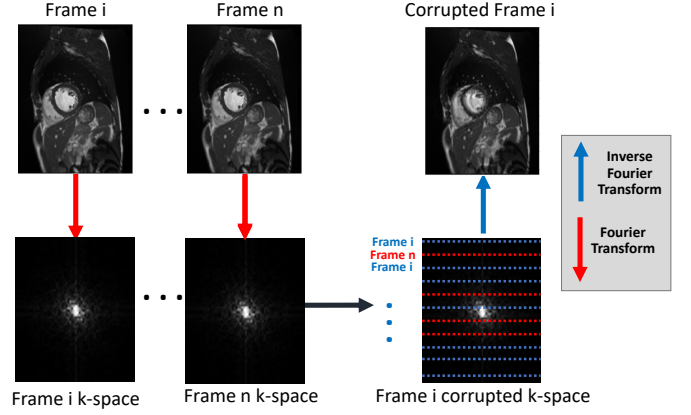


Fig. 2. K-space corruption for synthetic motion artefact generation in k-space. The Fourier transform of each image frame is applied to generate the k-space representation of each image. We replace k-space lines with lines from different temporal frames to generate corruptions.

We evaluate our approach using a subset of the UK Biobank data set [32]. The subset consists of short-axis cine CMR images of 4000 subjects and was chosen so as to exclude any images with quality issues such as image artefacts, missing axial slices and was visually verified by an expert cardiologist. The short-axis images have an in-plane image resolution of  $1.8 \times 1.8 \text{ mm}^2$  with a slice thickness of 8.0 mm and a slice gap of 2 mm. A short-axis image stack typically consists of approximately 10-12 image slices and covers the full heart. Each cardiac cycle consists of 50 time frames, and every other frame (25 frames) balanced steady-state free precession (bSSFP) magnitude images of the mid-ventricular slice were used for analysis. All images were cropped to  $176 \times 132$  image size, centred at the myocardium using the technique described in [18] to have consistent image matrices. Details of the image acquisition protocol can be found in [32].

#### A. Synthetic image artefact generation

From the high quality subset of the UK Biobank data set, we generated k-space corrupted data in order to simulate motion artefacts. The UK Biobank data set was acquired using Cartesian sampling and we follow a Cartesian k-space corruption strategy to generate synthetic but realistic motion artefacts [33]. We first transform each 2D short axis sequence to the Fourier domain and change 1 in  $z$  Cartesian sampling lines to the corresponding lines from other cardiac phases in order to mimic cardiac motion artefacts. By using different values for  $z$ , we are able to generate cardiac motion artefacts with different severities. In Figure 2 we show an example of the generation of a corrupted frame  $i$  from the original frame  $i$  using information from the k-space data of other temporal frames. We add a random frame offset  $j$  when replacing the lines.

### IV. METHODS

In this section we first describe the unified framework for image artefact detection, correction and segmentation. Then,

we provide details of the neural network architectures used for each task. Finally, we introduce our joint loss function and the optimisation scheme.

#### A. Architecture

The overall architecture of our network is illustrated in Figure 3. The proposed framework consists of 3 sub-networks and 3 corresponding loss function terms, which we detail below.

#### B. Image motion artefact detection

The proposed artefact correction network architecture consists of two building blocks as visualised in Fig. 4 and as described in [4]: 1) a k-space line detection network to define the data consistency term; 2) a recurrent neural network architecture to correct image artefacts.

The proposed artefact detection CNN consists of eight layers as visualised in Fig. 4. The architecture of our network follows a similar architecture to the one in [34], which was originally developed for video classification using a spatio-temporal 3D CNN. In our case, we use the third dimension as the time component and 2D+time mid-ventricular sequences for classification of corrupted k-space lines. The input is an intensity normalised  $176 \times 132$  CMR images with 25 time frames with complex input treated as an additional channel. The network has 4 convolutional layers and 4 pooling layers, 1 fully-connected layer and a softmax loss layer to predict artefact-corrupted k-space lines. After each convolutional layer, a ReLU activation is used. We then apply pooling on each feature map to reduce the filter responses to a lower dimension. We apply dropout with a probability of 0.2 at all convolutional layers and after the first fully connected layer to enforce regularisation. All of these convolutional layers are applied with appropriate padding of 2 and stride of 1.

#### C. Motion corrected image reconstruction

In our algorithmic setup we utilise a convolutional recurrent neural network (CRNN) architecture [20] as the reconstruction network. The CRNN is designed to reconstruct CMR images from undersampled k-space data by jointly exploiting the dependencies of the temporal sequences as well as the iterative nature of traditional regularised MR reconstruction. In addition, spatio-temporal dependencies are simultaneously learned by exploiting bidirectional recurrent hidden connections across time sequences. The network consists of a bi-directional recurrent neural network for exploiting temporal information, and convolutional recurrent layers to propagate information between iterations.

However, we note that our framework is flexible and, in principle, other published reconstruction networks could be used in place of this network. The CRNN network was chosen due its capability to incorporate information from different temporal frames, which is instrumental in correcting k-space based artefacts.

#### D. Image Segmentation

Our segmentation network is a classical U-net segmentation network [5], which is known to perform well on the mid-ventricular segmentation task in high quality images [35]. The details of the network are illustrated in Fig. 5. We chose to use a simple and well-established segmentation model in order to allow us to evaluate the influence of different strategies for combining motion-corrected reconstruction with segmentation (see Section V-B).

#### E. Loss function

Our loss function incorporates terms from all three sub-networks with the overall loss function defined as:

$$\mathcal{L}_{\text{total}} = (1 - \lambda)\mathcal{L}_{\text{segmentation}} + \lambda\mathcal{L}_{\text{correction}}$$

where  $\mathcal{L}_{\text{correction}}$  refers to the joint image correction loss and  $\mathcal{L}_{\text{segmentation}}$  refers to the segmentation loss.  $\lambda$  is a weighting parameter, which controls the influence of both terms on the total loss.

Our correction loss is a combination of image reconstruction loss and a cross-entropy loss:

$$\mathcal{L}_{\text{correction}} = \gamma\mathcal{L}_{\text{detection}} + (1 - \gamma)\mathcal{L}_{\text{reconstruction}}$$

The reconstruction loss is computed using the mean square error, defined as:

$$\mathcal{L}_{\text{reconstruction}} = \frac{1}{N_p} \sum_{p=0}^{N_p} (I_x - I_y)^2$$

where  $N_p$  denotes the total number of pixels in images  $I_x$  and  $I_y$ . The detection loss is the cross entropy loss, defined as:

$$\mathcal{L}_{\text{detection}}(pr, y) = \frac{-1}{N_l} (y \log(pr) + (1 - y) \log(1 - pr))$$

where  $y$  is a binary indicator (0 or 1) indicating if a k-space line is corrupted or not and  $pr$  is the predicted probability of the line being uncorrupted.  $N_l$  denotes the total number of k-space lines in an image.

Finally, the segmentation loss is the pixel-wise cross entropy loss:

$$\mathcal{L}_{\text{segmentation}}(y_{\text{pred}}, y_{\text{true}}) = - \sum_{\text{classes}} y_{\text{true}} \log(y_{\text{pred}})$$

where  $y_{\text{pred}}$  is the probability of a segmentation label belonging to a class and  $y_{\text{true}}$  is the ground truth segmentation label.

#### F. Implementation details

During training, a batch-size of 10 2D+time sequences was used due to memory constraints. We used the Adam optimiser, whose momentum was set to 0.9 and the learning rate was  $5 \times 10^{-4}$ .

The parameters of the convolutional and fully-connected layers were initialised from a zero mean, unit standard deviation Gaussian distribution. In each trial, training was continued until the network converged. Convergence was defined as

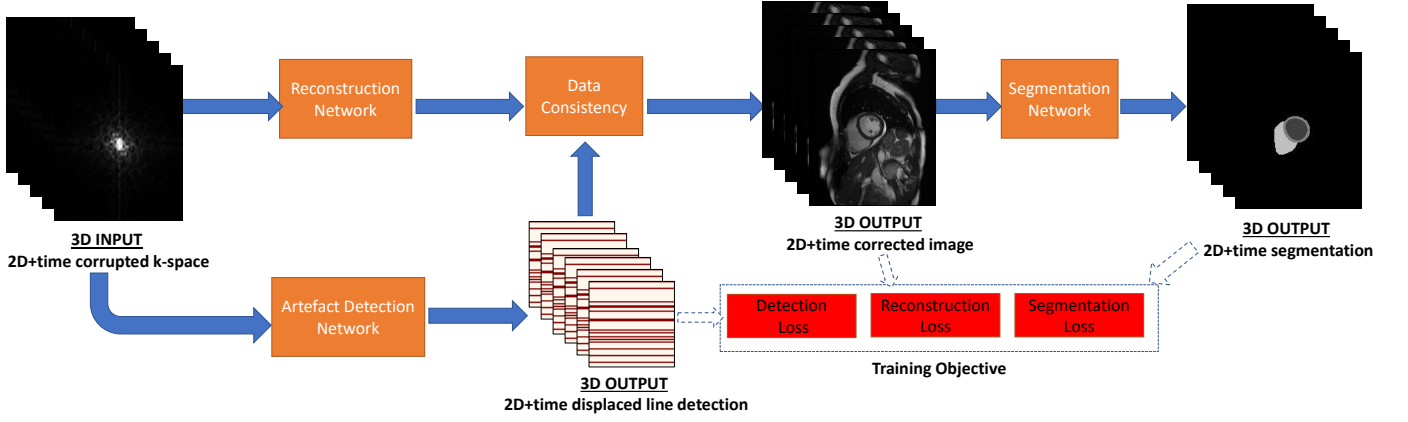


Fig. 3. The 2D+time CNN architecture for motion artefact detection, reconstruction and segmentation. Our network detects and corrects image artefacts and outputs a motion corrected image sequence, which is also segmented by a segmentation network. The segmentation gets fed back and further improves on the reconstruction in our training setup.

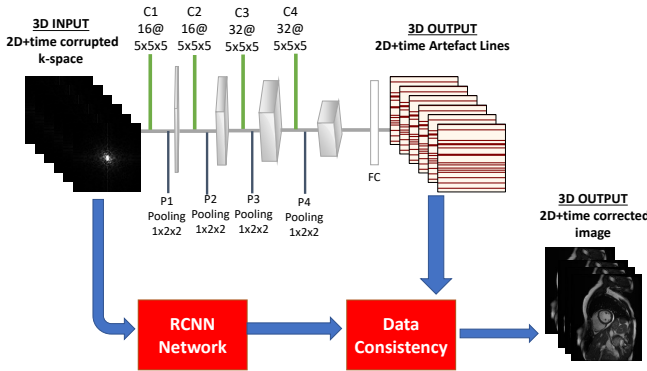


Fig. 4. The CNN architecture for motion artefact correction. Our network is able to detect displaced acquisitions in k-space and uses a data consistency term to achieve high image quality.

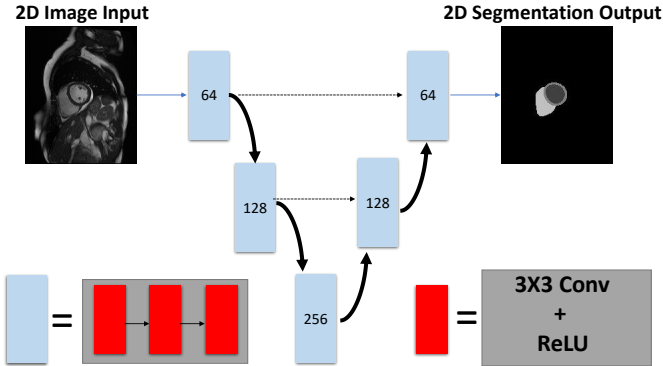


Fig. 5. Diagram of the U-net architecture used for segmentation of 2D temporal sequences. Numbers correspond to the number of channels, and dotted arrows correspond to feature concatenation.

a state in which no substantial progress was observed in the training loss. One percent improvement is considered significant in our training setup. Parameters were optimised using a grid-search among all parameters. We used the Pytorch framework for implementation. Training the network took around 15 hours on a NVIDIA Quadro P6000 GPU.

Classification of a single 2D+time image sequence took less than 1s.

## V. EXPERIMENTS AND RESULTS

Four sets of experiments were performed. The first set of experiments (Section V-B) aimed to compare the performance of different algorithmic approaches for automatic motion artefact correction and segmentation, while the second set of experiments (Section V-C) aimed at comparing different design choices for the correction network. To show the potential of our method as a global image reconstructor, we also report the results of each network using uncorrupted k-space data as input in Section V-D. Finally, the experiments in Section V-F validate the proposed network architecture for a prospective case study in which we utilise raw k-space data from a CMR acquisition. Before describing the experiments in detail, we first describe the evaluation measures used.

### A. Evaluation metrics and methods of comparison

Image quality is evaluated with Mean Absolute Error (MAE), Peak Signal to Noise Ratio (PSNR) and Structural Similarity Index (SSIM). For evaluating the prospective data, where no ground truth is available, the Sharpness Index (SI) [36] is used to evaluate performance.

MAE is defined as:

$$\text{MAE} = \frac{1}{N_p} \sum_{p=0}^{N_p} \|(I_x(p) - I_y(p))\|$$

where  $p$  denotes each pixel and  $N_p$  denotes the total number of pixels in images  $I_x$  and  $I_y$ .

PSNR is defined as:

$$\text{PSNR} = 20 \log_{10}(\max(I)) - 10 \log_{10} \left( \frac{1}{N_p} \sum_{p=0}^{N_p} (I_x(p) - I_y(p))^2 \right)$$

where  $\max(I)$  denotes the maximum intensity value in the ground truth image.



The SSIM between two images is defined as follows for any image regions  $x$  and  $y$ :

$$\text{SSIM}(p) = \frac{(2\mu_x\mu_y + c_1)(2\sigma_{xy} + c_2)}{(\mu_x^2 + \mu_y^2 + c_1)(\sigma_x^2 + \sigma_y^2 + c_2)}$$

where  $\mu_x$  and  $\mu_y$  are the average intensities for regions  $x$  and  $y$ ,  $\sigma_x$  and  $\sigma_y$  are variance values for regions  $x$  and  $y$ ,  $\sigma_{xy}$  is the covariance of regions  $x$  and  $y$  and  $c_1$  and  $c_2$  are constant values for stabilising the denominator.

The SI between two images is defined as:

$$SI(u) = \log_{10} \Phi \frac{\mu - TV(u)}{\sigma}$$

Where  $\mu = E[TV(I)]$  is the expectation of the total variation of the image and  $\sigma = Var[TV(I)]$  is the corresponding variance.

We computed the Dice overlap measure for evaluating segmentations, which is defined between two regions  $A$  and  $B$  as:

$$D(A, B) = \frac{2\|A \cap B\|}{\|A\| + \|B\|}.$$

### B. Architecture comparison

Two sets of tests were performed for deciding on the best architectural design to correct and segment CMR images with image artefacts. To decide on the best architecture, we tested several designs (as illustrated in Figure 6), while keeping the total number of parameters in the models the same: 1) a single U-net for image correction and image segmentation (U-net); 2) a U-net with 2 output channels for the corrected image and the final segmentation output (U-net 2-channel); and 3) two serial U-nets to first output a corrected image and then segment the image (Cascaded U-nets). To evaluate all designs, we used a training set of 3000, a validation set of 500 and a test set of 500 2D+time CMR images from the UK Biobank subset described in Section III.

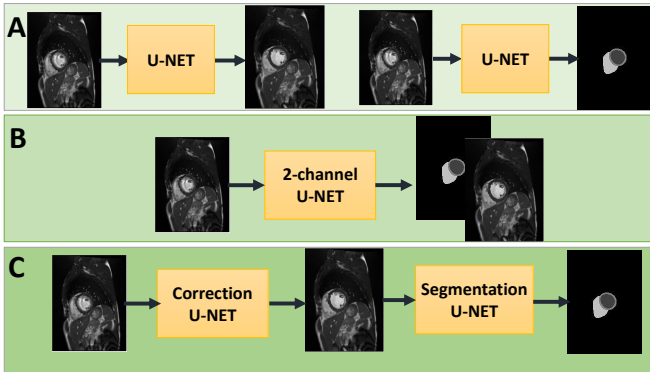


Fig. 6. Compared architectures for image motion artefact correction and segmentation: (a) a single U-net, which addresses the tasks of correction and segmentation separately, (b) a single U-net with 2-channel outputs, (c) two-consecutive networks, where first U-net corrects the image artefacts and the second one segments the corrected images. All architectures have low quality images as input.

In Table I, we report the segmentation results of this experiment. We also report the best achievable result, which

TABLE I  
DICE SEGMENTATION OVERLAP OF THE ALGORITHM OUTPUTS WITH THE GROUND TRUTH SEGMENTATION (MANUAL DELINEATION OF THE GOOD QUALITY IMAGE). THE PROPOSED ARCHITECTURE ACHIEVES HIGH DICE OVERLAP FOR THE LEFT VENTRICLE (LV), MYOCARDIUM (MYO) AND RIGHT VENTRICLE (RV) REGIONS.

Methods	LV	Myo	RV
U-net-Top	0.985	0.958	0.944
U-net-Baseline	0.944	0.871	0.896
Single U-net	0.968	0.926	0.927
U-net 2-channel	0.925	0.925	0.926
<b>Cascaded U-nets</b>	<b>0.970</b>	<b>0.933</b>	<b>0.932</b>

TABLE II  
IMAGE QUALITY OF THE ALGORITHM OUTPUTS WITH THE GOOD QUALITY ACQUISITION. THE CONSECUTIVE NETWORK ARCHITECTURE ACHIEVES THE BEST IMAGE QUALITY.

Methods	MAE	PSNR	SSIM	SI
Corrupted-Baseline	0.061	20.691	0.761	56.072
U-net	0.058	25.095	0.756	69.737
U-net 2-channel	0.057	25.238	0.775	71.084
<b>Cascaded U-nets</b>	<b>0.055</b>	<b>26.190</b>	<b>0.784</b>	<b>73.107</b>

employs a single U-net model but does not use any corrupted images during training or testing (U-net-Top). Also, using the same model without further training we segmented the poor quality images to establish a baseline performance (U-net-Baseline). Our experiments show that the best segmentation can be achieved by using two serial networks and training them end-to-end, which motivates our design choice for the remaining experiments.

In Table II, we report the image quality results of this experiment. In this table, we also report the original quality of the corrupted images as a baseline (Corrupted-Baseline). The results show that the best image quality can be achieved by using two serial networks and training them end-to-end, confirming the segmentation findings in Table I.

### C. Correction technique analysis

Having decided on the architecture to utilise for jointly addressing the reconstruction and segmentation tasks, we next aim to illustrate the benefit of our proposed technique. In Tables III and IV we report the segmentation and image quality results respectively for this experiment. The results show that the our novel technique, where we replace the correction U-net, improves image quality and final segmentation outputs.

Example results from this experiment are shown in Figure 7. The proposed technique can generate high quality images with low difference compared to the original images, with improvements in particular at edges. Moreover, the improved

TABLE III  
DICE SEGMENTATION OVERLAP OF THE ALGORITHM OUTPUTS WITH THE GROUND TRUTH SEGMENTATION (MANUAL DELINEATION OF THE GOOD QUALITY IMAGE). THE PROPOSED ARCHITECTURE ACHIEVES HIGH DICE OVERLAP FOR THE LEFT VENTRICLE (LV), MYOCARDIUM (MYO) AND RIGHT VENTRICLE (RV) REGIONS.

Methods	LV	Myo	RV
Cascaded U-nets	0.970	0.933	0.932
<b>Proposed</b>	<b>0.972</b>	<b>0.942</b>	<b>0.940</b>

TABLE IV

IMAGE QUALITY OF THE ALGORITHM OUTPUTS WITH THE GOOD QUALITY ACQUISITION. THE PROPOSED NETWORK CAN ACHIEVE HIGH PSNR AND SSIM.

Methods	MAE	PSNR	SSIM	SI
Cascaded U-nets	0.055	26.190	0.784	69.737
<b>Proposed</b>	<b>0.050</b>	<b>29.125</b>	<b>0.813</b>	<b>76.219</b>

image quality results in higher quality segmentations, clearly delineating the myocardium, LV and RV with high accuracy.

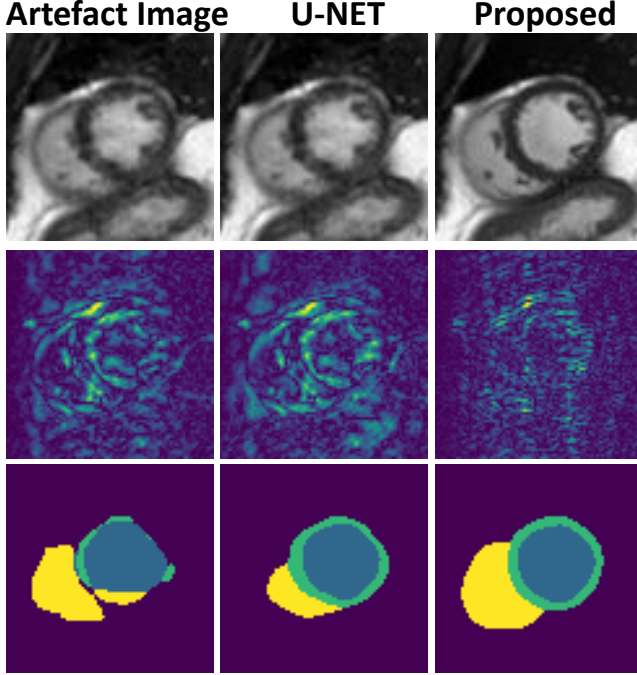


Fig. 7. Example results for proposed architecture and 2 separately trained U-nets. Top row shows a synthetic low quality cine CMR image (left), the corrected image output of 2 separately trained U-nets (middle) and the corrected image output of our proposed method (right). The second row shows the differences with corresponding good quality image for each case. The bottom row shows the generated segmentation outputs.

#### D. Uncorrupted results

We also used the trained models to test our framework on the original uncorrupted data, in order to demonstrate its potential as a general image reconstruction/segmentation tool. Table V presents the results achieved with each algorithm. Our proposed technique diminishes the quality of images least and therefore shows great potential to be used as a global image reconstructor.

#### E. Parameter analysis

Next, we repeated the training of our proposed technique for different  $\lambda$  values to highlight the importance of this parameter on image quality and segmentation. We used a range of values from 0 to 1 in steps of 0.05, and the results are shown in Figure 8. The parameter  $\lambda$  weights the image reconstruction loss and segmentation loss and accordingly can be used to tune for either higher image quality or higher segmentation quality in our algorithmic framework depending on clinical choices.

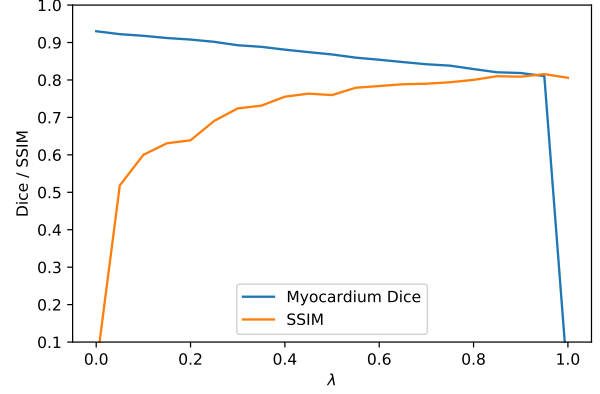


Fig. 8. Influence of the  $\lambda$  parameter on segmentation accuracy (Dice) and image quality (SSIM). The weight plays an important role in adjusting our pipeline to put more emphasis on one of the two tasks.

#### F. Prospective raw k-space data analysis

Finally, we investigated the performance of our method in a prospective study, where we acquired fully sampled raw k-space data of mid-ventricular short axis slices with 25 phases from a healthy volunteer under three different circumstances. The first acquisition was a breath-hold image, cardiac-triggered using the volunteer's ECG signal, which results in a high quality image. Then we acquired 2 different acquisitions with mistriggering artefacts. The mistriggering arose from the use of synthetic ECG signals featuring 60 and 70 beats per minute (bpm) respectively, rather than the real ECG of the volunteer. The results reported below are averaged over these two mistriggered acquisitions.

In Table VI, we compare the image quality results achieved by different algorithms in comparison to our proposed method, in terms of the no-reference image quality metrics SI and PSNR. The baseline refers to the image acquisition with artefacts without applying any correction algorithm. U-net refers to the two consecutive U-net architecture introduced in Section V-B. The increased image quality is illustrated in Figure 9. The high quality image generated with our framework is similar to the image acquired without mis-triggering. This demonstrates that our proposed methodology can be applied on the raw k-space data prospectively and can achieve high image quality.

In Table VII, we compare the image segmentation results achieved with U-net and the proposed technique. In this case, the ground truth segmentation was generated by an expert clinician using the breath-hold image. The baseline refers to the overlap between a manual segmentation of the artefact image and the ground truth on the breath-hold image. The proposed technique achieves high quality segmentation for myocardium, LV and RV blood pool as illustrated in Figure 9.

## VI. DISCUSSION AND CONCLUSION

We have presented an extensive study on automatic cardiac motion artefact detection, correction and segmentation in an end-to-end deep learning architecture, which can be used as

TABLE V

MEAN IMAGE QUALITY RESULTS OF IMAGE QUALITY CORRECTION FOR MOTION ARTEFACTS FOR UNCORRUPTED INPUTS. UNCORRUPTED RESULTS USE THE CORRECT K-SPACE AS INPUT. THE RESULTS INDICATE THE POTENTIAL OF OUR METHOD TO BE USED AS A GLOBAL IMAGE RECONSTRUCTION FRAMEWORK.

Methods	Segmentation			Image Quality			
	LV	Myo	RV	MAE	PSNR	SSIM	SI
U-net	0.920	0.852	0.887	0.017	35.279	0.891	72.176
U-net 2-channel	0.938	0.886	0.897	0.013	36.305	0.887	78.182
Cascaded U-nets	0.957	0.894	0.912	0.009	37.344	0.923	80.910
<b>Proposed</b>	<b>0.980</b>	<b>0.945</b>	<b>0.932</b>	<b>0.005</b>	<b>39.92</b>	<b>0.952</b>	<b>86.904</b>

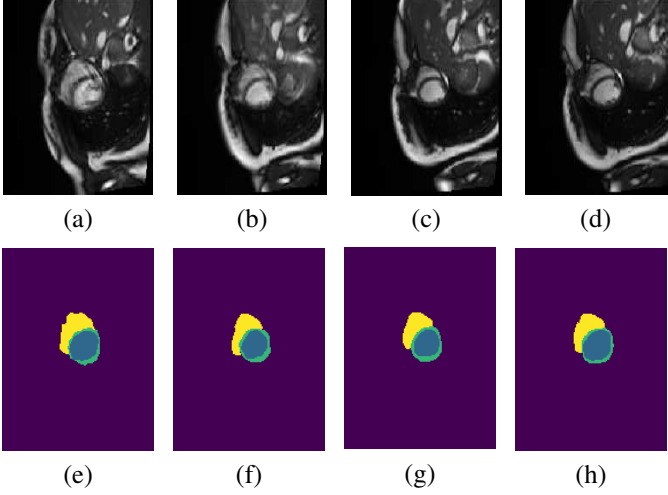


Fig. 9. Prospective study results. Artefact are generated by applying mis-triggering during acquisition (a), which results in low quality segmentations (e). Raw k-space data is corrected using two U-nets for correction (b) and segmentation (f). Our proposed method produces a high quality image output (c) and a high quality segmentation (g), which is comparable to image acquisition without mis-triggering (d) and ground truth segmentation (h).

TABLE VI

IMAGE QUALITY OF THE ALGORITHM OUTPUTS WITH THE GOOD QUALITY ACQUISITION. THE TRAINED NETWORK ACHIEVES HIGH PSNR AND SHARPNESS FOR THE DATA FROM RAW K-SPACE IN A PROSPECTIVE STUDY.

Methods	PSNR	SI
Baseline	0.623	58.940
Cascaded U-nets	0.753	61.800
<b>Proposed</b>	<b>0.793</b>	<b>63.890</b>

a global image reconstructor. First, we generated synthetic artefacts from high quality data to train our algorithm and we tested different network architectures to address the tasks of artefact correction and downstream segmentation. Our fundamental contribution in this paper is to address

TABLE VII

DICE SEGMENTATION OVERLAP OF THE ALGORITHM OUTPUTS WITH THE GROUND TRUTH SEGMENTATION (MANUAL DELINEATION OF THE GOOD QUALITY IMAGE). THE PROPOSED ARCHITECTURE ACHIEVES HIGH DICE OVERLAP IN PROSPECTIVE SETUP FOR LEFT VENTRICLE (LV), MYOCARDIUM (MYO) AND RIGHT VENTRICLE (RV) REGION.

Methods	LV	Myo	RV
Baseline	0.889	0.561	0.905
Cascaded U-nets	0.895	0.651	0.918
<b>Proposed</b>	<b>0.964</b>	<b>0.775</b>	<b>0.933</b>

image artefact detection, correction and segmentation jointly, resulting in a network architecture that can output both good quality image reconstructions and segmentations. We have also investigated the use of our algorithm in a prospective study to truly evaluate the clinical potential of our framework.

One key observation of our work is the superiority of two consecutive networks for achieving high quality images and image segmentations, compared to 2-channel networks. Moreover, we tested various strategies for image artefact correction and proposed a methodology to correct low quality images directly from k-space, which is improved by back-propagating the segmentation loss. It is interesting to observe that a joint network using a combination of detection, correction and segmentation losses improves the performance in terms of both image and segmentation quality. Moreover, the proposed method did not decrease image/segmentation performance on high quality data, which illustrates the success of our method in correctly detecting cases without motion artefacts. Finally, employing a weighting to each loss, the user can tune the network to perform any of the three tasks more accurately, which gives the user the option to choose between high image quality and high segmentation accuracy according to their needs.

In future, we would like to include more prospective cases in a real clinical setup to truly evaluate the performance of our algorithm with different MR vendors and field strengths. Moreover, investigation of basal and apical slice quality, which exhibits a slightly different anatomy and challenge, is an important future direction. In this work, we deliberately used existing network architectures and loss functions to enable us to focus our evaluation on the influence of our joint detection, correction and segmentation framework. One additional avenue of improvement is to investigate novel architectures tailored to the segmentation problem at hand.

The UK Biobank is a controlled study, which uses the general public as a cohort. The real utility of the proposed architecture will be in a clinical setting. Patients who require a CMR scan are likely to have cardiac conditions such as arrhythmias, and may have difficulties with breath-holding. Therefore, image artefacts are likely to be more common. With the successful translation of our architecture in clinical setups, high diagnostic image and segmentation quality can be offered consistently. Furthermore, MR images of other organs can suffer from artefacts and require accurate segmentations,



and we believe that a similar paradigm could be applied for those.

In conclusion, this work represents an important contribution to CMR image reconstruction. Our novel idea of detecting and correcting artefacts from k-space for high segmentation accuracy has been shown to improve both reconstructed image quality and segmentation quality. In the current environment of the increasing use of imaging in clinical practice, as well as the emergence of large population data cohorts which include imaging, our proposed global image reconstructor and segmenter can ensure high quality outputs independent of such motion artefacts.

## REFERENCES

- [1] I. Oksuz, J. Clough, W. Bai, B. Ruijsink, E. Puyol-Antón, G. Cruz, C. Prieto, A. P. King, and J. A. Schnabel, "High-quality segmentation of low quality cardiac MR images using k-space artefact correction," in *MIDL*, ser. Proceedings of Machine Learning Research, vol. 102. PMLR, 2019, pp. 380–389.
- [2] B. Ruijsink, E. Puyol-Antón, I. Oksuz, M. Sinclair, W. Bai, J. A. Schnabel, R. Razavi, and A. P. King, "Fully automated, quality-controlled cardiac analysis from cmr: Validation and large-scale application to characterize cardiac function." *JACC. Cardiovascular imaging*, Jul. 2019.
- [3] P. F. Ferreira, P. D. Gatehouse, R. H. Mohiaddin, and D. N. Firmin, "Cardiovascular magnetic resonance artefacts," *Journal of Cardiovascular Magnetic Resonance*, vol. 15, no. 1, p. 41, 2013.
- [4] I. Oksuz, J. Clough, B. Ruijsink, E. Puyol-Antón, A. Bustin, G. Cruz, C. Prieto, D. Rueckert, A. P. King, and J. A. Schnabel, "Detection and correction of cardiac mr motion artefacts during reconstruction from k-space," *arXiv*, 2019.
- [5] O. Ronneberger, P. Fischer, and T. Brox, "U-net: Convolutional networks for biomedical image segmentation," in *MICCAI*. Springer, 2015, pp. 234–241.
- [6] L. Kang, P. Ye, Y. Li, and D. Doermann, "Convolutional neural networks for no-reference image quality assessment," in *Proceedings of the IEEE conference on computer vision and pattern recognition*, 2014, pp. 1733–1740.
- [7] L. S. Chow and R. Paramesran, "Review of medical image quality assessment," *Biomedical Signal Processing and Control*, vol. 27, pp. 145–154, 2016.
- [8] J. P. Woodard and M. P. Carley-Spencer, "No-reference image quality metrics for structural MRI," *Neuroinformatics*, vol. 4, no. 3, pp. 243–262, 2006.
- [9] L. Wu, J.-Z. Cheng, S. Li, B. Lei, T. Wang, and D. Ni, "Fuiqa: Fetal ultrasound image quality assessment with deep convolutional networks," *IEEE Transactions on Cybernetics*, vol. 47, no. 5, pp. 1336–1349, 2017.
- [10] A. H. Abdi, C. Luong, T. Tsang, G. Allan, S. Nouranian, J. Jue, D. Hawley, S. Fleming, K. Gin, J. Swift *et al.*, "Automatic quality assessment of apical four-chamber echocardiograms using deep convolutional neural networks," in *Proc. SPIE*, vol. 10133, 2017, pp. 101 330S–1.
- [11] T. Küstner, A. Liebgott, L. Mauch, P. Martirosian, F. Bamberg, K. Nikolaou, B. Yang, F. Schick, and S. Gatidis, "Automated reference-free detection of motion artifacts in magnetic resonance images," *Magnetic Resonance Materials in Physics, Biology and Medicine*, vol. 31, no. 2, pp. 243–256, 2018.
- [12] T. Kuestner, S. Gatidis, A. Liebgott, M. Schwartz, L. Mauch, P. Martirosian, H. Schmidt, N. F. Schwenzer, K. Nikolaou, F. Bamberg *et al.*, "A machine-learning framework for automatic reference-free quality assessment in mri," *arXiv preprint arXiv:1806.09602*, 2018.
- [13] L. Zhang, A. Gooya, and A. F. Frangi, "Semi-supervised assessment of incomplete lv coverage in cardiac mri using generative adversarial nets," in *SASHIMI*, 2017, pp. 61–68.
- [14] G. Tarroni, O. Oktay, W. Bai, A. Schuh, H. Suzuki, J. Passerat-Palmbach, B. Glocker, P. M. Matthews, and D. Rueckert, "Learning-based quality control for cardiac mr images," *arXiv preprint arXiv:1803.09354*, 2018.
- [15] R. Robinson, V. V. Valindria, W. Bai, O. Oktay, B. Kainz, H. Suzuki, M. M. Sanghvi, N. Aung, J. M. Paiva, F. Zemrak *et al.*, "Automated quality control in image segmentation: application to the uk biobank cardiovascular magnetic resonance imaging study," *Journal of Cardiovascular Magnetic Resonance*, vol. 21, no. 1, p. 18, 2019.
- [16] X. Alba, K. Lekadir, M. Pereaez, P. Medrano-Gracia, A. A. Young, and A. F. Frangi, "Automatic initialization and quality control of large-scale cardiac mri segmentations," *Medical Image Analysis*, vol. 43, pp. 129 – 141, 2018.
- [17] B. Lorch, G. Vaillant, C. Baumgartner, W. Bai, D. Rueckert, and A. Maier, "Automated detection of motion artefacts in mr imaging using decision forests," *Journal of medical engineering*, vol. 2017, 2017.
- [18] I. Oksuz, B. Ruijsink, E. Puyol-Antón, J. R. Clough, G. Cruz, A. Bustin, C. Prieto, R. Botnar, D. Rueckert, J. A. Schnabel *et al.*, "Automatic cnn-based detection of cardiac mr motion artefacts using k-space data augmentation and curriculum learning," *Medical image analysis*, vol. 55, pp. 136–147, Jul. 2019.
- [19] Y. Han and J. C. Ye, "k-space deep learning for accelerated MRI," *CoRR*, vol. abs/1805.03779, 2018.
- [20] C. Qin, W. Bai, J. Schlemper, S. E. Petersen, S. K. Piechnik, S. Neubauer, and D. Rueckert, "Joint motion estimation and segmentation from undersampled cardiac mr image," *Machine Learning for Medical Image Reconstruction*, Jan. 2018.
- [21] J. Schlemper, J. Caballero, J. V. Hajnal, A. N. Price, and D. Rueckert, "A deep cascade of convolutional neural networks for dynamic mr image reconstruction," *IEEE transactions on Medical Imaging*, vol. 37, no. 2, pp. 491–503, 2017.
- [22] A. Hauptmann, S. Arridge, F. Lucka, V. Muthurangu, and J. A. Steeden, "Real-time cardiovascular mr with spatio-temporal artifact suppression using deep learning-proof of concept in congenital heart disease," *Magnetic resonance in medicine*, vol. 81, pp. 1143–1156, Feb. 2019.
- [23] D. Liu, B. Wen, X. Liu, Z. Wang, and T. S. Huang, "When image denoising meets high-level vision tasks: A deep learning approach," *arXiv*, 2017.
- [24] S. Wang, B. Wen, J. Wu, D. Tao, and Z. Wang, "Segmentation-aware image denoising without knowing true segmentation," *arXiv*, 2019.
- [25] G. J. S. Litjens, T. Kooi, B. E. Bejnordi, A. A. A. Setio, F. Ciompi, M. Ghafoorian, J. A. W. M. van der Laak, B. van Ginneken, and C. I. Sánchez, "A survey on deep learning in medical image analysis," *Medical Image Analysis*, vol. 42, pp. 60–88, 2017.
- [26] M. Shao, S. Han, A. Carass, X. Li, A. M. Blitz, J. L. Prince, and L. M. Ellingsen, "Shortcomings of ventricle segmentation using deep convolutional networks," *Understanding and Interpreting Machine Learning in MICCAI*, Jan. 2018.
- [27] Q. Huang, D. Yang, J. Yi, L. Axel, and D. Metaxas, "Fr-net: Joint reconstruction and segmentation in compressed sensing cardiac mri," *Functional Imaging and Modeling of the Heart*, Jan. 2019.
- [28] Q. Huang, X. Chen, D. Metaxas, and M. S. Nadar, "Brain segmentation from k-space with end-to-end recurrent attention network," *arXiv*, 2018.
- [29] J. Schlemper, O. Oktay, W. Bai, D. C. Castro, J. Duan, C. Qin, J. V. Hajnal, and D. Rueckert, "Cardiac mr segmentation from undersampled k-space using deep latent representation learning," *MICCAI*, Jan. 2018.
- [30] O. Oktay, E. Ferrante, K. Kamnitsas, M. Heinrich, W. Bai, J. Caballero, S. A. Cook, A. de Marvao, T. Dawes, D. P. O'Regan, B. Kainz, B. Glocker, and D. Rueckert, "Anatomically constrained neural networks (ACNNs): Application to cardiac image enhancement and segmentation," *IEEE Transactions on Medical Imaging*, vol. 37, no. 2, pp. 384–395, Feb. 2018.
- [31] L. Sun, Z. Fan, Y. Huang, X. Ding, and J. Paisley, "Joint cs-mri reconstruction and segmentation with a unified deep network," *arXiv*, 2018.
- [32] S. E. Petersen, P. M. Matthews, J. M. Francis, M. D. Robson, F. Zemrak, R. Boubertakh, A. A. Young, S. Hudson, P. Weale, S. Garratt *et al.*, "UK biobanks cardiovascular magnetic resonance protocol," *Journal of Cardiovascular Magnetic Resonance*, vol. 18, no. 1, p. 8, 2016.
- [33] I. Oksuz, J. Clough, A. Bustin, G. Cruz, C. Prieto, R. Botnar, D. Rueckert, J. A. Schnabel, and A. P. King, "Cardiac mr motion artefact correction from k-space using deep learning-based reconstruction," *Machine Learning for Medical Image Reconstruction*, Jan. 2018.
- [34] D. Tran, L. Bourdev, R. Fergus, L. Torresani, and M. Paluri, "Learning spatiotemporal features with 3d convolutional networks," in *Proceedings of the IEEE international conference on computer vision*, 2015, pp. 4489–4497.
- [35] W. Bai, M. Sinclair, G. Tarroni, O. Oktay, M. Rajchl, G. Vaillant, A. M. Lee, N. Aung, E. Lukaschuk, M. M. Sanghvi *et al.*, "Automated cardiovascular magnetic resonance image analysis with fully convolutional networks," *Journal of Cardiovascular Magnetic Resonance*, vol. 20, no. 1, p. 65, 2018.
- [36] G. Blanchet and L. Moisan, "An explicit sharpness index related to global phase coherence," in *ICASSP*. IEEE, 2012, pp. 1065–1068.